Faraday Discussions

Cite this: *Faraday Discuss.*, 2023, **245**, 467

PAPER

Thermal behavior of astrophysical amorphous molecular ices

Murthy S. Gudipati, *[a] Benjamin Fleury, [b] Robert Wagner, [c] Bryana L. Henderson, [a] Kathrin Altwegg [d] and Martin Rubin [d]

Received 20th February 2023, Accepted 7th March 2023
DOI: 10.1039/d3fd00048f

Ice is a major component of astrophysical environments – from interstellar molecular clouds through protoplanetary disks to evolved solar systems. Ice and complex organic matter coexist in these environments as well, and it is thought primordial ice brought the molecules of life to Earth four billion years ago, which could have kickstarted the origin of life on Earth. To understand the journey of ice and organics from their origins to becoming a part of evolved planetary systems, it is important to complement high spatial and spectral resolution telescopes such as JWST with laboratory experimental studies that provide deeper insight into the processes that occur in these astrophysical environments. Our laboratory studies are aimed at providing this knowledge. In this article we present simultaneous mass spectrometric and infrared spectroscopic investigation on how molecular ice mixtures behave at different temperatures and how this information is critical to interpret observational data from protoplanetary disks as well as comets. We find that amorphous to crystalline water ice transformation is the most critical phenomenon that differentiates between outgassing of trapped volatiles such as CO_2 *vs.* outgassing of pure molecular ice domains of the same in a mixed molecular ice. Crystalline water ice is found to trap only a small fraction of other volatiles (<5%), indicating ice grain composition in astrophysical and planetary environments must be different depending on whether the ice is in amorphous phase or transformed into crystalline phase, even if the crystalline ice undergoes radiation-induced amorphization subsequently. Crystallization of water ice is a key differentiator for many ices in astronomical environments as well as in our Solar System.

Introduction

Astrochemistry is aimed at simulating astrophysical environments to predict chemical processes as well as providing their underlying mechanisms in these

[a]*Science Division, Jet Propulsion Laboratory, California Institute of Technology, 4800 Oak Grove Drive, Pasadena, CA 91109, USA. E-mail: murthy.gudipati@jpl.nasa.gov*
[b]*Univ Paris Est Creteil and Université Paris Cité, CNRS, LISA, F-94010 Créteil, France*
[c]*Institute of Meteorology and Climate Research, Karlsruhe Institute of Technology, Karlsruhe, Germany*
[d]*Physikalisches Institut, University of Bern, Sidlerstrasse 5, CH-3012 Bern, Switzerland*

environments. As JWST continues to provide outstanding data at better spatial and spectral resolution and sensitivity than the previous telescopic measurements,[1–4] the need to obtain laboratory data at higher resolution is now more important than ever before. In addition to higher spectral resolution that enables better separation of individual absorption/emission bands and higher spatial resolution of observations that provides better contrast of the observed objects (whether interstellar molecular clouds or protoplanetary disks or other solar system objects), we need a better understanding of the effect of temperature, pressure, and local radiation in these environments that are often spatially heterogeneous. Small temperature variations could have a significant effect on the ice *vs.* gas-phase composition in these environments.[5,6] Temperature measurements in astrophysical environments are still averaged through the line of sight and often need to be approximated. For this reason, if laboratory studies could provide better handle on the effect of temperature on the ice/gas partitions, we should be able to use these data to better constrain temperatures of local astrophysical environments. Observations with higher spatial resolution can then be better interpreted using laboratory data.

In protoplanetary environments, ice-lines are drawn at various radial and lateral distances from the protostar.[6–8] However, these lines are dictated by not only ice composition and its phase (amorphous or crystalline), but also the exact temperature of the local environment. For this reason, we focused in our study on outgassing of mixed molecular ices and their composition at various temperatures. In protoplanetary disks, though temperature decreases with radial distance, volatile and supervolatile molecular species (with respect to water) would form pure ices or mixed ices trapped in water and other ices based on their local abundances. It is still not clear whether ice particles form in the protoplanetary disks freshly or retain their interstellar ice grain properties as they accrete on to a protoplanetary disk during its formation. Though radial transportation is used in many models, how far the grains and gas are transported and whether transport occurs primarily in one direction or both directions (high to low and low to high temperatures) are still open questions,[9,10] particularly, when gas-phase observations are used as a proxy for ice composition.[11] It is also assumed that the icy grains in the protoplanetary disks become a part of cometary nuclei retaining their chemical, structural, and compositional integrity.[12–14] Thus, there is an effort to correlate cometary outgassing (reflecting thermal evolution of a comet during its travel around the Sun) with the ice grain composition of protoplanetary disks. In order to gain better constraints on interpreting observational data from icy environments – be they interstellar, protoplanetary, or cometary nuclei – we need a wide range of laboratory data. We conducted temperature programmed desorption (TPD) studies of mixed molecular ices by means of simultaneous mass spectrometry of outgassed molecules and infrared spectroscopy of mixed molecular ices. We also carried out calorimetric study of macroscopic water ice. Our experiments provide some of these critically needed data and understanding of the processes involved, complement existing experimental data as discussed in the following, and provide a deeper understanding of the role of local temperature on the ice physics.

Experimental

All the experiments were conducted at the Ice Spectroscopy Laboratory (ISL) of the Jet Propulsion Laboratory. We used standard Temperature Programmed Desorption (TPD) methods to determine sublimation of mixed molecular ices at various starting mixing ratios. The experimental station (named Himalaya) used for this work is shown in Fig. 1.

TPD of mixed molecular ices

Molecules used here are CO, O_2, CO_2, and H_2O as a realistic representative of supervolatiles (CO and O_2), and volatiles (CO_2) in water ice. We chose much higher mixing ratios such that the volatiles are in "excess" compared to what have been observed in astrophysical or cometary ices.[15–18] This was deliberately done to

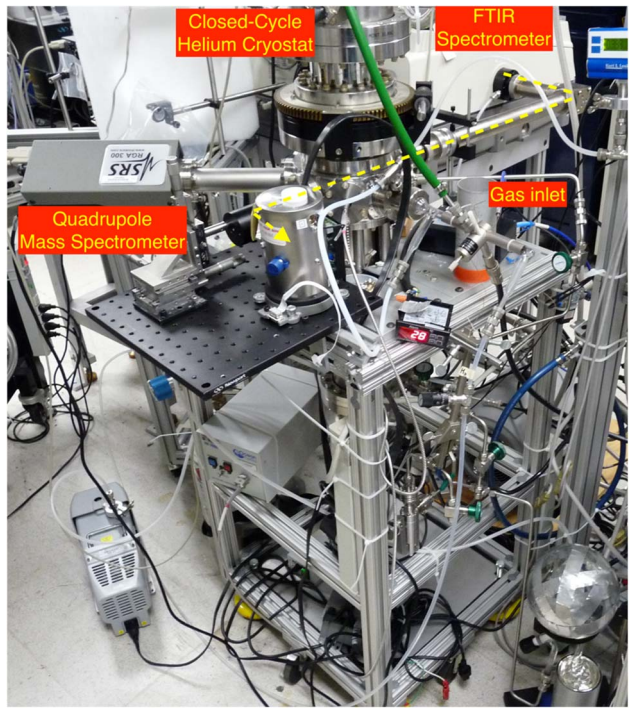

Fig. 1 Experimental station (named Himalaya) that is used to conduct TPD-MS, TPD-IR, and calorimetry experiments at the Ice Spectroscopy Laboratory (ISL) of the Jet Propulsion Laboratory (JPL). FTIR (Thermo-Nicolet 6700) beam is guided through Ni-coated tubes with high-throughput reflecting mirror and passed through the sapphire optical window mounted on a sample holder at the end of the closed-cycle helium cryostat in the vacuum chamber. The transmitted IR beam is focused with a parabolic gold-coated mirror on to the MCT-A detector. Once ice is deposited, the sample is then rotated to be perpendicular to the IR beam and held in that position for the entire TPD experiment. Also mounted on the vacuum chamber is the quadrupole mass spectrometer (Stanford Research Instruments, SRS 300) which is equipped with an electron multiplier. In this configuration we have been able to simultaneously record FTIR and mass spectra at a given temperature during the TPD experiments.

ensure that there are pure volatile and supervolatile ice domains in the mixed molecular ices. This method differs slightly from previous methods,[19,20] where either observed mixing ratios were used for mixed molecular ices or layered ices,[21–33] or pure ices were studied through TPD.[34,35] In astrophysical environments it is unlikely that pure supervolatile ice grains exist where no other molecule is present in the ice grains, such as pure CO ice, though pure CO ice domains could exist in an ice grain that contains other volatiles as well. Properties of such mixed-molecular ices or layered ices also depend upon whether these ice grains travelled from cold to warmer regions of the protoplanetary disk or *vice versa*. It is easy to imagine grains moving from the inner protoplanetary disk to the outer, which would lead to less volatile molecules to condense first forming layered ice grains with supervolatiles condensing on the top of the ice grain. The situation is more complex if the movement is from colder to warmer regions as the supervolatiles that are trapped within the less volatile molecular ices only survive in that ice grain. For this reason, we think our molecular mixing ratio provides a more realistic representative of pure ice domains in mixed molecular ice grains and complements data so far available on other ice compositions mentioned earlier.

All the ice mixtures were deposited at 10 K on a sapphire substrate at normal incidence for a duration of 3–6 min at a background pressure of $\sim 1 \times 10^{-6}$ mbar. The end of the vapor deposition tube (1/4-inch outer diameter stainless steel) was kept $\sim$2 inches away from the sapphire optical window that was cooled with a Sumitomo (SHI-4-15, Janis Research) closed-cycle helium cryostat that reaches a minimum of 4.2 K. Calibration studies done on water ice under these conditions show the ice films are of $\sim$250 nm (about 1000 monolayers) in thickness. Initial mixing ratios were controlled based on pressure in the ice chamber determined by an inverted magnetron pressure gauge (Agilent Varian IMG-300). We did not use the mass spectrometer to adjust the mixing ratios because of fragmentation of CO_2 to CO that interferes with the exact ratios. Final mixing ratios are determined from the FTIR spectral integrated intensities normalized to the respective band strengths (see Results section) of the individual molecules.

The temperature ramp was held at 0.5 K min^{-1}. Our Lakeshore (Model 340) temperature controller allows for a ramp rate as slow as 0.1 K min^{-1}, but the long duration experiments introduce artefacts such as background deposition that may lead to erroneous results. We experimented with faster ramp rates (1 K min^{-1}) and found that the rate did not show significant effect on the TPD-mass spectrometry (TPD-MS) of these ices. Most of the experiments were done with 0.5 K min^{-1} heating rate to ensure better equilibration of ice at any given temperature and better applicability of TPD data to typical astrophysical environments.

Desorption of molecular volatiles during TPD was quantified through quadrupole ion mass spectrometry (MS) using a Stanford Research Systems (SRS RGA-300) quadrupole mass spectrometer and infrared (IR) spectroscopy using a Thermo-Nicolet 6700 FTIR spectrometer equipped with a KBr beam splitter and an external liquid-nitrogen cooled MCT-A detector. IR spectroscopy provides independent and complementary data on the desorption process in terms of molecules remaining in the ice phase, whereas mass spectrometry provides composition of desorbed molecules in vacuum. We found that this combination of techniques was particularly useful in cases where species are less-efficiently pumped by the turbomolecular pump (*i.e.*, CO molecules) and thus can be over-represented in the mass spectra, or for those that are unable to be quantified by the infrared spectra alone (*i.e.*, N_2 and O_2

molecules). With IR spectroscopy, we were also able to track a slight increase in the IR absorption of the H_2O ice band as the temperature is ramped due to sublimation from other parts of the cryostat and recondensation on the sapphire window.

Ionization of gases in the mass spectrometer was done at 70 eV. Electron-impact ionization cross-sections at 70 eV for these molecules are taken from NIST data (O_2 = 2.441 Å^2; CO = 2.516 Å^2; CO_2 = 3.521 Å^2; H_2O = 2.275 Å^2). Integrated mass spectral data were then normalized with respect to the CO_2 ionization cross-section to obtain molecular mixing ratios of deposited gas mixture (which in turn represents closely the ice composition determined through infrared spectroscopy). The scaling factors used are: O_2 (1.44); CO (1.4); CO_2 (1); H_2O (1.55). We note here that the CO mass peak at 28 m/z has contribution from N_2 (which can be estimated to be about 8 times the partial pressure of N detected at 14 m/z) as well as ionization fragmentation of CO_2 to CO, which is about 10% of CO_2 partial pressure. These and slow pumping of CO by turbomolecular pumps cause difficulties to quantitatively interpret the CO mixing ratio in the outgassing under our experimental conditions.

Using the integrated IR spectral absorbances, the relative molecular abundance was calculated using band strengths from the literature[36–39] as follows: CO (1.1×10^{-17} cm per molecule); CO_2 (7.7×10^{-17} cm per molecule); H_2O (1.6×10^{-16} cm per molecule). Please note that O_2 is IR inactive, and we rely upon mass spectrometry for O_2 mixing ratios. Further, we conducted calorimetry using the same conventional closed-cycle cryostat that is also used for the above mentioned TPD studies.

Calorimetry of pure H_2O ice

For the calorimetry experiments, we deposited macroscopic amounts of pure water at 10 K to form amorphous ice. Our goal was to capture the amorphous to crystalline phase transition of pure H_2O ice and determine if there were differences in temperature range or any dependence on ice thickness on the crystallization of amorphous ice during TPD. For these experiments, we made an internal calibration between two temperature-measuring silicon diodes, the first diode (SD1) is mounted at the end of the heating tape where the sample holder is connected to the closed-cycle cryostat and the second silicon diode (SD2) is mounted at the bottom of the sample holder (see Fig. 2). Amorphous ice was directly deposited on the copper sample holder where the SD2 is located for different durations. The water vapor inlet tube was brought about 5 mm closer to the SD2 location of the sample holder to avoid ice formation on the entire sample holder, but to limit it at the SD2 location. First, we ran a pre-programmed 2 K min^{-1} reference ramp prior to ice deposition using the Lakeshore temperature controller's temperature ramping with PID (proportional, integral, derivative) control. To obtain a smooth heating ramp devoid of the oscillations inherent in the PID control, we fitted the recorded time-dependent heater wattage values with a three-exponential fit and used these values to prescribe the heating ramp for the ice experiments. If there were no changes in the heat absorbed or released by the ice, at each pre-programmed ramping stage, the temperatures of both the diodes SD1 and SD2 would have read the same as without the sample. However, if there were to be heat released due to the exothermic amorphous to crystalline phase transition, the SD2 would read a higher temperature than SD1 and the ratio SD2/SD1 would increase. Similarly, for

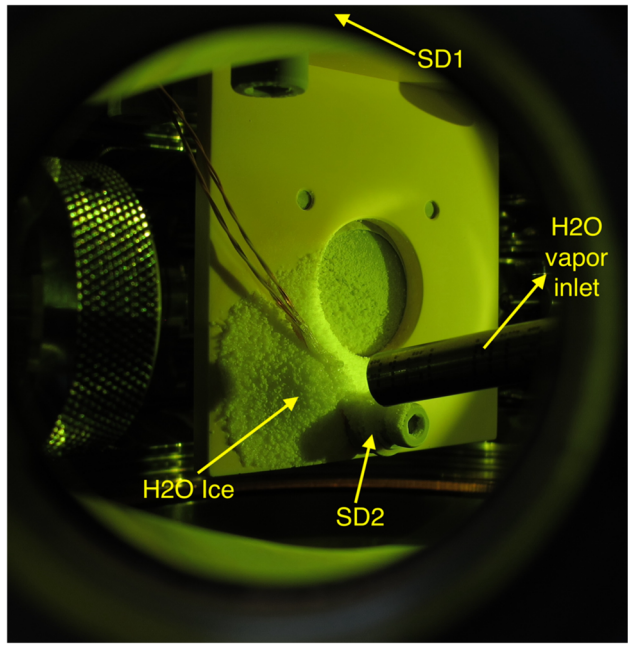

Fig. 2 Configuration of calorimetry on conventional closed-cycle helium cryostat used for ice TPD-MS and TPD-IR experiments. The locations of the Silicon Diode (SD) temperature sensors are shown. SD1, which cannot be seen in this photo, is mounted at the top of the ice sample holder that is connected to the end of the closed-cycle helium cryostat. SD2 is mounted at the bottom of the sample holder, which is made of oxygen-free copper. Also seen is the optical window mounted between the copper sample holder, on which normally ice is deposited for TPD experiments. The water vapor inlet is mounted closer to the sample holder and directed to the bottom part to ensure ice deposition is predominantly localized close to SD2.

an endothermic phase transition, this ratio would decrease. Indeed, subtle changes were measured corresponding to exothermic ice crystallization around 140 K and endothermic ice sublimation around 190 K. The ice samples deposited were estimated to be a few milligrams and the heating ramp was conducted at the maximum power setting on the heater controller at 100 W, starting at 35% of the output at 10 K and ending at ~90% at 200 K. Despite the high heater wattage needed to work against the cooling power, we were able to measure extremely small exothermic and endothermic peaks because we have used the two temperature sensor diodes located apart from each other that would otherwise have exactly the same conditions except for instantaneous minuscule differences in temperature. This is almost like weighing an elephant with and without a sparrow on it! But it indeed worked quantitatively as will be presented in the results section.

Results

TPD of mixed molecular ices

We studied several mixed molecular ices, including two component $CO:CO_2$, three component $CO:O_2:CO_2$, and four component $CO:O_2:CO_2:H_2O$ ices. We

also varied the mixing ratios, except the CO to O_2 ratio was kept constant close to 1. In the TPD-MS, we followed gas-phase N (proxy of N_2 that comes at the same m/z as CO at 28; N : N_2 peak ratio from NIST Webbook is ~12 : 100), CO, O_2, CO_2, CO_3 (that could be an impurity in CO gas cylinders through reaction of CO with O_2), and H_2O. Some of these desorption mass spectral plots are shown in Fig. 3–7 along with their counterpart from integration of the FTIR spectra. In Fig. 8, integrated mass spectral data, of outgassed volatiles trapped in amorphous water ice (>90 K) that are released during amorphous to crystalline ice transition ~140 K (black bars) and trapped in crystalline water ice (>145 K) that are released along with subliming water (orange bars), are shown as bar graphs. Full range mass spectra and infrared spectra for four component mixed molecular ice are shown in Fig. 9 and 10. Our TPD-MS profiles are qualitatively in agreement with earlier work, especially pure and mixed-molecular ices containing H_2O, CO, CO_2, CH_3OH and NH_3,[19] and H_2O, CO, CO_2 and CH_4.[40] In all the experiments we conducted, most of the CO either exists as a pure CO ice domain or CO is outgassed prior to the start of CO_2 outgassing, even if CO is trapped in CO_2 ice, except with CO : O_2 : CO_2 : H_2O mixed molecular ices. During the formation of water-dominant amorphous ice, all the other volatiles are trapped to some extent within the amorphous ice. We also observed some entrapment of CO_2 in pure CO or O_2 ice domains evident from CO_2 outgassing along with CO and O_2, both of which have similar sublimation temperatures. N_2 sublimation starts after CO sublimation

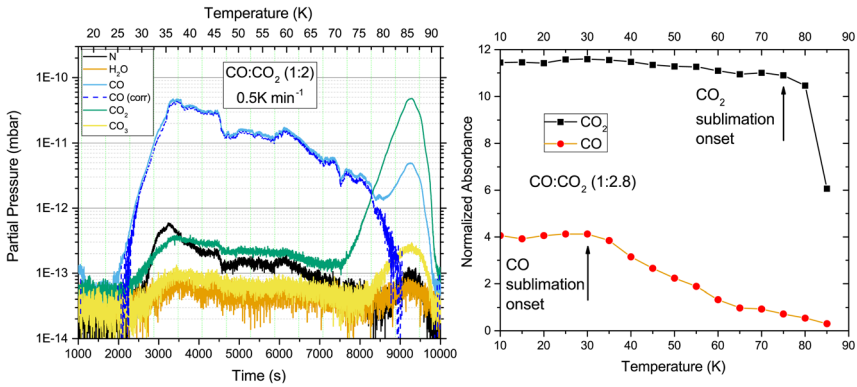

Fig. 3 TPD-MS profiles (left) and integrated TPD-IR absorption intensities that are normalized to respective band-strengths (right) of a two-component CO : CO_2 ice deposited at 10 K and heated at 0.5 K min^{-1}. While the TPD-MS data show an onset of CO sublimation at ~25 K, FTIR spectra show observable sublimation starting after 30 K. N_2 sublimation (with N as the proxy) is offset by ~5 K. A small amount of CO_2 that is trapped in CO ice is also sublimed along with CO between 30 K and 70 K. Only a small fraction of CO (~10%) remains trapped in CO_2 ice at 70 K, the onset of CO_2 sublimation, as indicated by the IR data. Please note that CO_2 fragmentation in the mass spectrometer results in around 10% of CO, which makes it difficult to quantify the mass spectra, as can be seen in the curve obtained after CO partial pressure correcting for CO_2 fragmentation and N_2 contribution. We skip this procedure in the rest of the TPD-MS profiles to keep clarity. Here, FTIR spectra are useful for quantification. For mass spectra the initial deposition chamber pressure ratios are given. For IR spectral data, the ratios obtained from integrated and normalized (to their band strengths) relative absorbances are given. Both are from the same ice and are simultaneously measured.

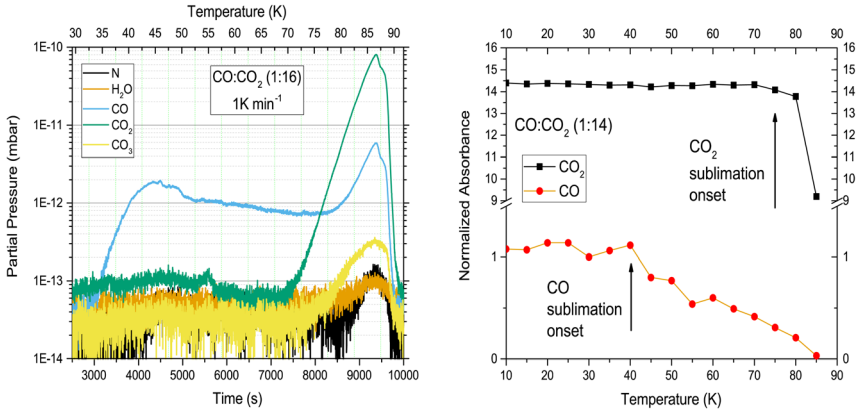

Fig. 4 TPD-MS profiles (left) and integrated TPD-IR absorption intensities (right) of two-component CO : CO_2 ice deposited at 10 K and heated at 1 K min^{-1}. Initial mixing ratio of CO is about 6–7% in CO_2 and most of the CO molecules are trapped in CO_2 ice. As a result, CO outgassing is delayed by about 10 K from the pure CO ice outgassing (refer to Fig. 3). About 3% of CO remained trapped in CO_2 ice at 70 K, the onset of CO_2 sublimation. For the rest of the information on the figure details, please refer to Fig. 3.

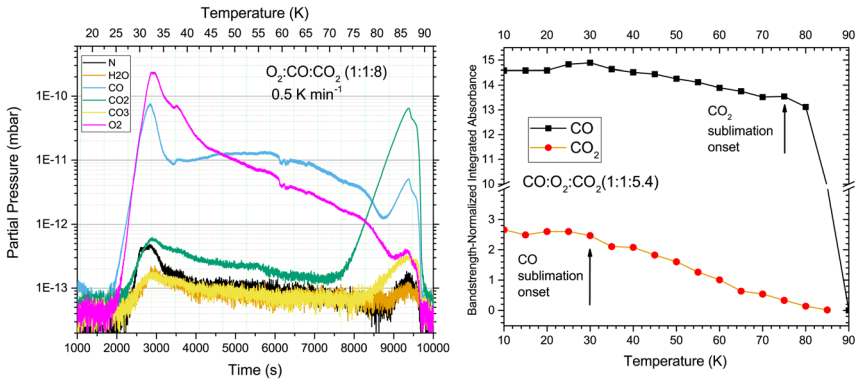

Fig. 5 TPD-MS profiles (left) and integrated TPD-IR absorption intensities (right) of three-component CO : O_2 : CO_2 ice deposited at 10 K and heated at 0.5 K min^{-1}. In the left figure, it can be seen that the O_2 partial pressure is slightly higher between 30 and 35 K and then drops rapidly while CO continues to remain in the vacuum chamber. Though the initial mixing ratio of CO : CO_2 is 1 : 5.4 (O_2 is IR inactive and assumed to be about the same mixing ratio as CO), most of the CO sublimes off between 30 K and 70 K, in agreement with the two-component experiments (Fig. 3 and 4), leaving only about 4% CO in CO_2 ice at the onset of CO_2 sublimation. For the rest of the information on the figure details, please refer to Fig. 3.

and along with O_2 sublimation, as inferred from tracing N in the TPD-MS profiles. Also, minor entrapment of CO and O_2 was observed in CO_2 ice domains as reflected in the CO_2 sublimation region of the TPD-MS profiles. Above 100 K, when all the excess pure ices of CO, O_2, and CO_2 are sublimed, the remaining ice on the substrate must be amorphous water ice and any residual volatiles/supervolatiles trapped in it. Indeed at ~130 K, we start observing another desorption event that

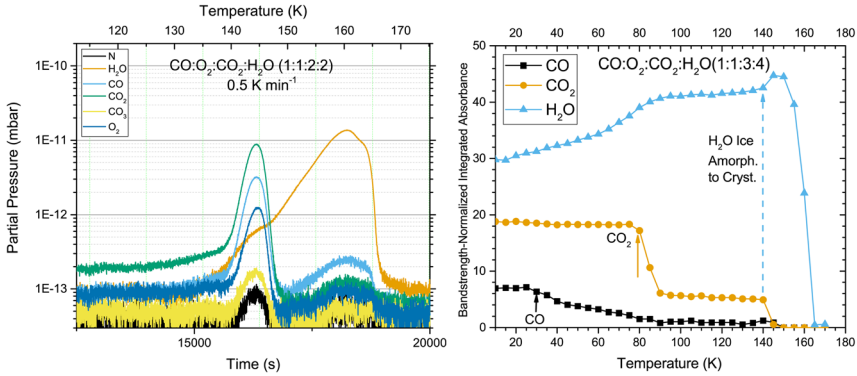

Fig. 6 Zoomed-in part of the TPD-MS profiles (left) and integrated TPD-IR absorption intensities (right) of four-component CO : O_2 : CO_2 : H_2O ice deposited at 10 K and heated at 0.5 K min^{-1}. In the left figure, we see between ~137 K and ~147 K a significant outgassing of trapped volatiles in amorphous water ice. In the right figure, we observe similar outgassing onset of CO (hence O_2 as well) at 30 K and gradual outgassing until CO_2 outgassing, which occurs between 70 K and 90 K. Above 90 K, the amount of CO trapped in the amorphous ice is far less than CO_2. The data confirm outgassing of almost all CO, O_2, and CO_2 during crystallization of amorphous ice. During water–ice sublimation only a few percent of these volatiles are still trapped. This experiment demonstrates that if crystalline water ice in astrophysical environments were to be formed, it could accommodate a maximum of 5% of other volatiles in its lattice. If crystalline water ice is observed along with other ices, they must have been formed separately after amorphous water ice has been crystallized (*i.e.*, subjected to temperatures above 120 K for a given amount of time, which is dependent on the maximum exposed temperature below 160 K under vacuum conditions). Please note that water ice integrated absorbance increases constantly and reaches its maximum around 150 K. This is less likely to be due to the increased band strength of water ice with temperature, but rather due to sublimation of a small amount of water from warmer parts of the cryostat and redeposition on the sapphire optical window. For the rest of the information on the figure details, please refer to Fig. 3.

maximizes at 145 K and completes at 150 K. During this period, a significant amount of all three volatiles CO, O_2, and CO_2 are released simultaneously into the gas-phase, along with a small amount of H_2O sublimation. We see consistently that more CO_2 is trapped in amorphous water ice than CO or O_2. From the integrated TPD-MS data we find that the sum of all trapped species in amorphous water ice is about 30%. Our data indicates that indeed amorphous water ice can trap significant amounts of other volatile species even at temperatures as high as 130 K. Interestingly, as soon as the temperature reaches 150 K all the trapped volatiles are desorbed and the amorphous to crystalline ice transformation is then complete as well. Above 150 K, water ice starts sublimation alone. At this point only an extremely small portion of other volatiles are trapped in the crystalline water ice, as evident from the desorption maxima around 160 K, where only about 2–3% of CO is seen to desorb along with H_2O. The rest of the molecules have even lower mixing ratios. We can use the TPD-MS and IR data of our experiments to backtrack ice composition at different temperatures.

Infrared spectra have also been simultaneously obtained and the discrepancies between IR and mass spectral data reveal values obtained for CO from

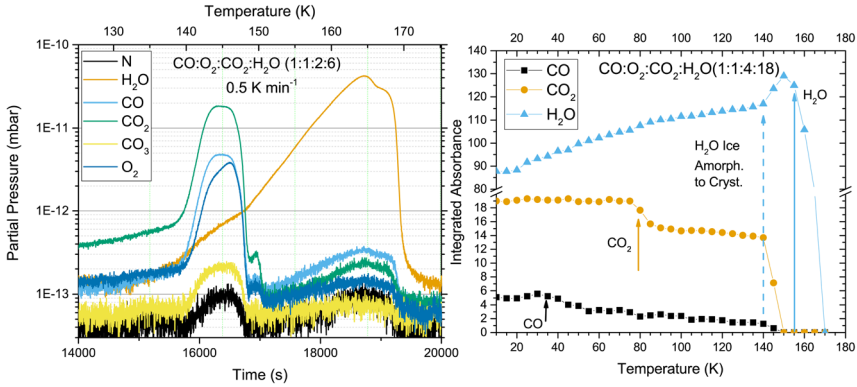

Fig. 7 Zoomed-in part of the TPD-MS profiles (left) and integrated TPD-IR absorption intensities (right) of a four-component $CO : O_2 : CO_2 : H_2O$ ice deposited at 10 K and heated at 0.5 K min^{-1}. In this experiment, we increased the mixing ratio of water to test whether there would be any change in the thermal or trapping behavior. We found no changes and, as expected, significant amounts of CO (O_2) and CO_2 were trapped in amorphous ice and released during crystallization. Otherwise, both the two four-component ice types behaved very similarly. Please refer to Fig. 6 and 3 for additional details.

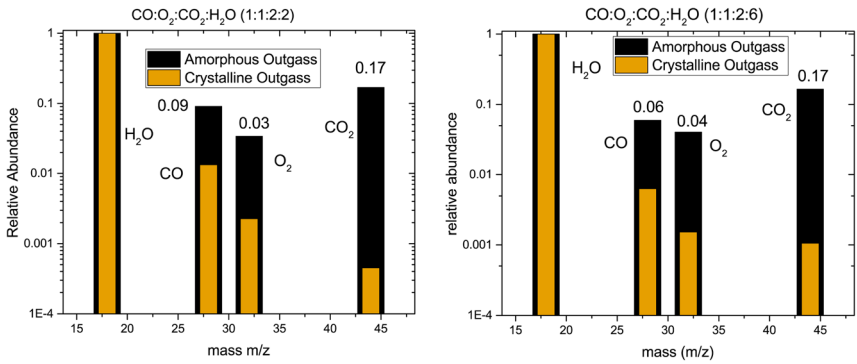

Fig. 8 Relative abundances with respect to H_2O calculated from integrated TPD-MS spectra (shown in Fig. 6 and 7) of four-component $CO : O_2 : CO_2 : H_2O$ ice deposited at 10 K and heated at 0.5 K min^{-1}. Volatiles CO, O_2, and CO_2 outgassed during crystallization of amorphous water ice between 130 K and 150 K normalized to the total water content are shown in black bars and the same for crystalline water ice outgassing between 150 K and 190 K shown in orange bars. In spite of different mixing ratios, in both experiments above 90 K, CO_2 is trapped in amorphous ice at an abundance of 17%, while CO and O_2 are much lower in abundance (6–9% and 3–4%, respectively). After amorphous ice crystallizes, the total amount of volatiles trapped is reduced to around 1%. Again, our experiments demonstrate that crystalline water ice does not trap significant amounts of volatiles.

mass spectral data alone cannot be quantitatively used due to the longer residence time of CO in the vacuum chamber. For example, total integrated TPD-MS partial pressure ratio of $CO : CO_2$ is $\sim 3 : 1$, whereas IR spectral data indicate a $CO : CO_2$ ratio of $1 : 2.8$ (Fig. 3). It is well known that conventional turbomolecular

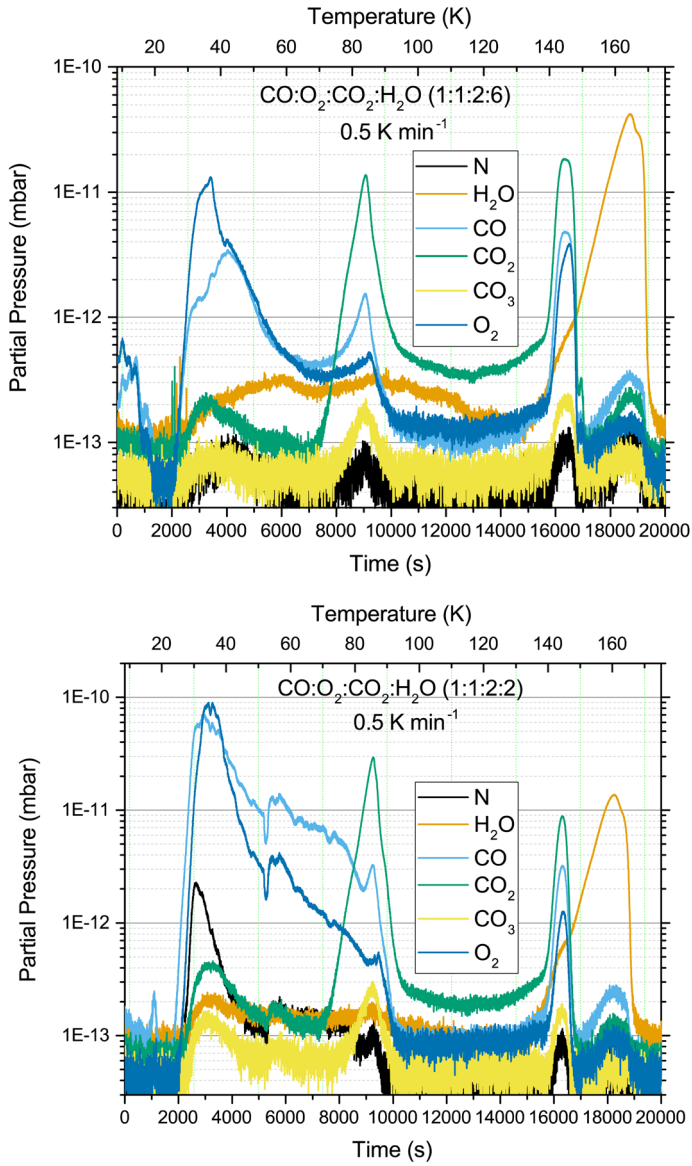

Fig. 9 Mass spectral profiles during TPD from 10 K to 190 K of four component mixed molecular ices CO : O_2 : CO_2 : H_2O.

pumps even at 10^{-9} mbar vacuum are less efficient at pumping CO. As a result, integrated mass spectra over-estimate CO outgassing. This is further complicated by continuous CO release from the ice into the vacuum that is clearly seen from the IR spectra of the ices (Fig. 3–7). In the astrochemistry community, the majority of the cryogenic systems are equipped with these turbomolecular pumps, at $\sim 10^{-9}$ mbar working pressures. As discussed below, under those conditions caution must be exercised in the interpretation of TPD-MS data alone.

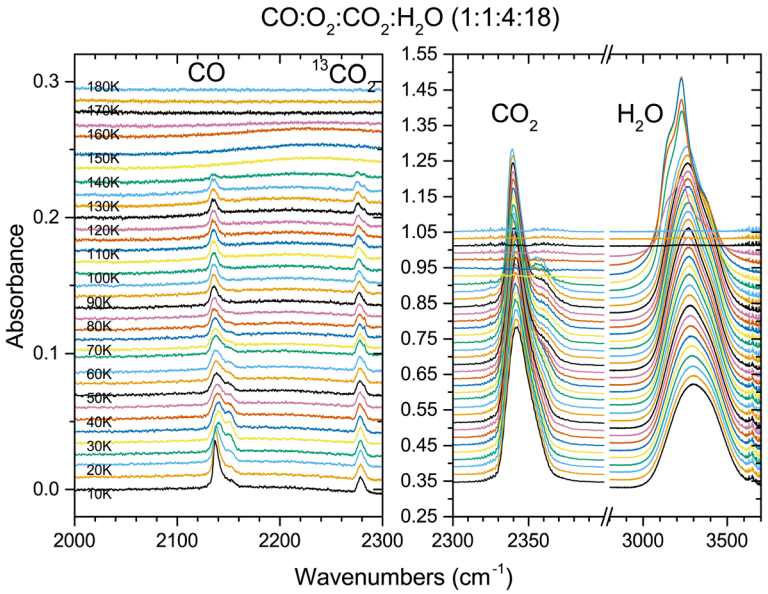

Fig. 10 FTIR absorbance spectra of four component CO : O_2 : CO_2 : H_2O mixed molecular ice during TPD. Spectra are stacked to provide clarity. CO absorption around 2140 cm^{-1} quickly splits into two components, the higher energy one disappearing by 90 K, indicating the lower energy part should be due to CO trapped in amorphous water–ice. CO_2 absorption at 2340 cm^{-1} starts as a single broad band and as the temperature increases a shoulder develops on the higher energy side, which becomes a clear band beyond CO_2 ice sublimation. Around 145 K all CO_2 sublimes and the amorphous water ice band centered around 3250 cm^{-1} develops into a three-band structure, typical of crystalline water ice. Around 185 K, all the water ice sublimes, leaving no residue behind.

Calorimetry of pure H_2O ice

In order to quantify the exothermicity of the amorphous to crystalline ice transition, we have relied on an internal standard, namely the heat of sublimation of crystalline ice. In our first experiment, where ice was deposited at 2–3 $\times$ 10^{-5} mbar for 900 min at a rate of 1 $\times$ 10^{-5} g min^{-1} (black line curve in Fig. 11), the endothermic sublimation as well as the exothermic crystallization are well behaved. Subsequently, we increased the time of deposition as shown in Fig. 11 and both the exotherm and endotherm peaks increased, with the sublimation endotherm out of bound with thicker ice sample. At this point, ice sublimation is so fast that the vacuum in the system raised significantly (to $\sim$1 $\times$ 10^{-3} mbar) and the data was no longer reliable. We excluded such data from calculating the sublimation enthalpy. From the literature, we took the sublimation endotherm to be 2830 kJ kg^{-1},[41] and multiplied it by the ratio of the integrated crystallization exotherm to the integrated sublimation endotherm. By this procedure, we obtained the heat of crystallization exotherm for amorphous ice to be 109 kJ kg^{-1}, 109 kJ kg^{-1}, 116 kJ kg^{-1}, and 138 kJ kg^{-1} for the four different experiments we conducted at different ice deposition durations ranging from 900 min to 5160 min, with an arithmetic mean and standard deviation of 118 $\pm$ 12 kJ kg^{-1}. This value is in very good agreement with the literature reports of $\sim$100 kJ

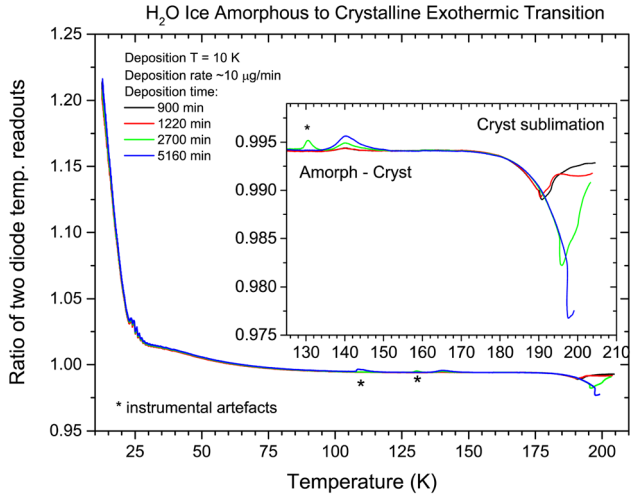

Fig. 11 Differential calorimetry during 2 K min^{-1} pure water ice annealing from amorphous to crystalline to sublimation transitions. Ratio of SD2/SD1 (SD = silicon diode for temperature readout) at various temperatures is plotted for four different ice experiments. SD2 is directly in contact with the ice, whereas SD1 acts as an internal reference at the top of the sample holder. For an exothermic phase transition, this ratio is higher and for an endothermic phase transition it is smaller with respect to a common baseline ratio. We consistently see an exothermic transition between 130 and 150 K with maximum at 140 K due to the amorphous to crystalline phase transition. This peak position remains independent of ice thickness, but the transition intensifies with thickness as expected (more ice deposition mass induces a greater heat release and larger differences in the temperatures read at SD1 and SD2). We also observe the endothermic sublimation transition with an onset around 170 K, which also intensifies with thickness. The sublimation onset is the same in all cases, but the sublimation maximum shifts depending on thickness, since it is a surface-driven phenomenon and it takes longer for thicker ices to complete the sublimation process. For thinner ice it maximizes at ~190 K, and moves to higher temperatures for thicker ice.

kg^{-1}.[42–45] Our method is simple and easy to implement for a wide range of equipment and ices.

Discussion

There are a few major take aways from our experiments presented here. The first one is that super volatiles CO, O_2, and N_2 (proxy N) can only exist in significant mixing ratios in interstellar, protoplanetary, and cometary ices that are extremely cold – at or less than 30 K. The second take away is that the exothermicity of amorphous to crystalline pure water ice transition is confirmed again. At the same time, we also found that irrespective of the ice thickness – whether a few hundred nanometers thin ice films or few hundred micrometers to millimeters thick ice grains – the amorphous to crystalline ice transition occurs within a narrow temperature range of 130 K to 150 K, with a maximum at ~140 K. Another experimental take away is that quantification of CO in the gas-phase under vacuum should be carefully conducted and should be verified by complementary experiments. Finally, conventional cryogenic systems with no additional

instrument modification can be used to carryout calorimetry of ices and we plan to extend our calorimetric studies to mixed-molecular ices in the future. In the following we discuss more in detail temperature ranges and their effect on the ice/gas composition.

Below 30 K

Most interstellar ices, protoplanetary ices at greater radial distances, and Oort Cloud comet interiors are expected to be at or below 30 K. Under these conditions, based on our data presented here, we can expect no outgassing of any supervolatiles such as CO, O_2, N_2 (CH_4, Ar *etc.*, by inference) either as pure ices or trapped in mixed molecular ices. So, supervolatile-rich ices should be present at temperatures below 30 K. We can approximately refer to this the CO ice line.

30–75 K

This is the temperature range one expects in protoplanetary disks at closer distances than the CO ice line mentioned above. These temperatures are also present as equilibrium temperatures of solar system icy bodies such as TNOs (Trans Neptune Objects) and Kuiper Belt Objects (KBOs), and Centaurs.[46,47] In these environments, the ice grains are expected to be depleted of significant amounts of supervolatiles CO, O_2, and N_2 (CH_4, Ar *etc.*, by inference), but still contain significant amounts of CO_2. For this reason, Jupiter family short-period comets that originate from KBOs and Centaurs should be significantly depleted of CO and other supervolatiles, but still retain high amounts of CO_2. In the protoplanetary disks, the ice grains accreting from the interstellar environment and moving radially into the inner disk would have significant amounts of CO_2, but otherwise be depleted in supervolatiles. From the TPD-MS and TPD-IR data presented here, we find that though significant amount of CO is outgassed early (below 50 K), CO continues to leave the ice-phase gradually until CO_2 starts sublimation. This indicates that some of the CO molecules, either trapped in CO_2 or existing as a CO ice domain covered by CO_2 ice, outgas at higher temperature. We should be cautious to over interpret this data, as this outgassing is expected to be both temperature and time dependent.

75–120 K

This temperature range leads to the loss of any excess pure CO_2 ice and any volatiles left behind are now completely trapped within amorphous water ice cages in the 4-component ices. In three and two component ices, where CO_2 is the dominant species, we observe very small amounts (<3%) of supervolatiles (including N_2, O_2, and CO) to outgas along with CO_2 (Fig. 3–5), indicating CO_2 ice has crystallized expelling other impurities well before its sublimation onset.[48] Centaurs, the precursors of Jupiter-family comets, could have their equilibrium temperatures in this range.[49,50]

120–150 K

This is the most critical temperature in astrophysical environments, and it is a point of no return, when amorphous water ices irreversibly undergo phase transition into crystalline water ice, during which process all the volatiles trapped

within the amorphous ice are released. Our experiments show that about 17% CO_2, ~9% CO, and ~4% O_2 are trapped in warm amorphous ices beyond 90 K – and these are released during ice crystallization between 130 K and 150 K. These values are close to the modeling work done recently to reproduce comet 67P/Churyumov–Gerasimenko nucleus properties.[51] It is expected that crystallization of amorphous water ice is slower at lower temperatures and faster as the temperatures approach 150 K.[52] This temperature region in protoplanetary disks should be narrow but clearly marked by crystalline water–ice features in the IR spectral observations. JWST should be able to detect these regions and constrain the temperatures. Comets should also show unusual CO_2-rich outgassing and H_2O inactivity in these temperature ranges. Indeed, such dichotomy is observed in the outgassing of many comets, including 67P/CG,[53–56] whereby subsolar regions with higher temperatures show H_2O outgassing (crystalline water ice sublimation – see below), whereas other regions with lower temperatures show enhanced CO_2 outgassing. It is very likely that amorphous water ice loaded with CO_2 and other volatiles, at depths where thermal equilibrium reaches ~130 K, eject these volatiles while undergoing crystallization. As a result, a significant amount of CO_2, CO, and other volatiles are observed from the regions where the surface temperatures are lower. Once crystallized, water ice from the same region, when temperatures are higher due to direct exposure to Sun, results in predominantly H_2O sublimation (and depleted in CO_2). Based on this laboratory observation alone, we can confidently conclude that cometary nuclei are predominantly made of amorphous water ice, at least deep inside the nucleus. We also note that presence of silicate dust and refractory organic mantle on short-period comets could further effect outgassing from comets.[53,54,57]

150–190 K

Above 150 K crystalline water ice starts to sublimate rapidly. Based on the thickness of the crystalline water ice film, sublimation could be complete at 170 K or above. The sublimation temperature also depends on the ambient pressure of the ice, with higher pressures shifting sublimation to higher temperatures. Such a scenario does not exist in low-pressure protoplanetary environments but could be present in the near sub-surface ices of the outer Solar System icy bodies and cometary near sub-surface ices, as a comet gets closer to its perihelion. The location of crystalline water ice sublimation in the protoplanetary disks is also designated as H_2O ice line that is closer to 150 K. However, based on the above-mentioned variables, it is possible that water ice could persist at higher temperatures.

If an accreted interstellar amorphous ice grain makes its journey through each of the ice lines in a protoplanetary disk, shedding away volatiles, the remaining material on these grains would be highly refractory (silicates and complex organics). If these grains or silicate dust from the inner protoplanetary disk were subsequently to move radially outwards, then the ice condensation on these grains will be layered (onion-like), with the non-volatiles such as H_2O condensing first, followed by other volatiles such as CO_2, and finally the supervolatiles such as CO. Thus, the composition of an ice grain – layered *vs.* intimately mixed – depends on whether it was formed within the protoplanetary disk or retained from interstellar grains.

The structural composition of these grains (layered *vs.* intimately mixed) plays an important role in the subsequent chemistry of these ices. Because highly energetic particles can deposit energy in ionization tracks as they penetrate through matter, reactions tend to occur with nearby species. As a result, any radiation-induced chemistry of protoplanetary-disk-formed ice grains should be different from interstellar ice grain chemistry.

Cometary nuclei have been puzzling researchers for decades. The recent Rosetta mission provided more insight into the outgassing properties of comet 67P/CG.[53] High porosity of cometary nuclei and large thermal gradients make predictions of cometary nucleus composition based on outgassing difficult. However, based on our data and earlier experimental work, we can provide some insight into cometary nuclei: (a) if the entire nucleus of a comet reaches its equilibrium temperature above 70 K, it would be unlikely that these comets contain regions of pure molecular ices of super volatiles such as CO, N_2, CH_4, *etc.* We observe continuous outgassing of CO from the mixed molecular ice above 30 K until CO_2 sublimation starts at 70 K. More laboratory work is needed to understand the long-term effect of temperature between 30 K and 70 K on the outgassing of these supervolatiles to determine if any of their pure ice domains would survive these temperatures. CO_2 ice domains are more likely to survive in the interiors of a comet nucleus with equilibrium temperature at or below 70 K, followed by trapped volatiles in amorphous H_2O ice below ~120 K. At closer heliocentric distances, where surface temperatures raise beyond H_2O ice sublimation temperatures below the dust mantle, outgassing properties of a comet would be most complex due to the thermal wave propagating deeper that results in not only sublimation of crystalline water ice, but also outgassing from amorphous to crystalline phase transition at deeper regions releasing significant amounts of trapped volatiles (also known as molecular volcanos on a comet).[33,58,59] However, at even greater depths CO_2 ice domains could start sublimation reaching the surface. However, the outgassing dichotomy of comets indicates that CO_2 is predominantly from relatively lower temperature regions on the surface compared to H_2O, indicating CO_2 outgassing could have contribution from all these processes. At larger heliocentric distances, however, H_2O amorphous-to-crystalline transition and sublimation are significantly suppressed, and it is expected that CO_2 ice domains dominate the outgassing in these regions. The Rosetta mission also found strong correlation between H_2O and O_2 outgassing, up to 5% mixing ratio of O_2.[60,61] In our experiments, we see a much smaller fraction of O_2 outgassing along with H_2O (see Fig. 8). One possibility is that cometary nuclei and their precursors may have been irradiated by cosmic rays over the past 4.6 billion years, resulting in radiation-induced trapping of O_2 in H_2O ice as has been seen on the surface of Galilean moons Europa, Ganymede, and Callisto[62] and experimentally demonstrated during ion irradiation of ice.[63] More laboratory studies are needed to understand complex thermal properties of cometary nuclei and their outgassing properties during their journey around the Sun.

In the outer Solar System, on icy satellites such as Europa and other Jovian and Saturnian moons, surface temperatures can vary between 150 K and 60 K depending on latitude and sub-solar regions.[64–67] Sub-solar equatorial regions sustain the highest possible temperatures, whereas polar regions remain cooler. Similarly, day and night temperatures also vary significantly. Under these conditions, water ice sublimation occurs from the crystalline ice phase into vapor,

forming a tenuous atmosphere. When the water vapor condenses on the surface, amorphous water ice could form in cold higher latitude regions or at lower latitudes on the night side. At temperatures below 70 K, this refrosting process could also lead to trapping of CO_2 if it is present in the atmosphere.

Conclusions

Temperature plays an important role in the compositional properties of astrophysical ices. Laboratory data under various conditions will provide better constraints on the interpretation of observational data, whether it is protoplanetary disks, comets, or other Solar System icy bodies. H_2O can co-condense with significant amounts of other volatiles and supervolatiles at very low temperatures (<30 K), whereas at warmer – above the CO_2 sublimation – temperature (>90 K), amorphous water ice has only a limited ability to trap volatiles, of which CO_2 has the highest mixing ratio. Crystallization of amorphous ice expels all the trapped volatiles around 130–150 K. This temperature region is the same, whether the ice grains are thin (a few hundred nanometers) or thick (a few hundred microns), based on our differential calorimetry experiments. Such a process could lead to outgassing of significant amounts of CO_2, whereas H_2O is still in the solid form. This important process likely explains the outgassing dichotomy observed in comets where CO_2 outgassing occurs from a different region of the comet than H_2O outgassing, which is predominantly from the subsolar regions. We also found that crystalline water ice traps only a small fraction of other volatiles (<5%), indicating ice grain composition in astrophysical and planetary environments must be different depending on whether the ice is in amorphous phase or transformed into crystalline phase. Once irreversibly transformed into crystalline phase, water ice is expected not to trap anymore volatiles, even if the crystalline ice undergoes radiation-induced amorphization subsequently. As for the protoplanetary disks, any radial mixing over long distances from the protostar could lead to entirely different ice compositions, namely layered ices, instead of the mixed molecular ices formed in the interstellar molecular clouds. The morphology of these layered ices could also lead to different radiation chemistry compared to mixed molecular ices. JWST observations should provide better insight and constraints on the formation and mobility of ice grains in protoplanetary environments.

Conflicts of interest

There are no conflicts to declare.

Acknowledgements

This research work was carried out at the Jet Propulsion Laboratory, California Institute of Technology, under a contract with the National Aeronautics and Space Administration. This research was enabled through funding to MSG from NASA SSW and DDAP Programs.

References

1 M. Jin, K. H. Lam, M. K. McClure, J. T. van Scheltinga, Z. Y. Li, A. Boogert, E. Herbst, S. W. Davis and R. T. Garrod, *Astrophys. J.*, 2022, **935**, 133.

2 B. Muller, B. M. Giuliano, A. Vasyunin, G. Fedoseev and P. Caselli, *Astron. Astrophys.*, 2022, **668**, A46.
3 S. Hinkley, A. L. Carter, S. Ray, A. Skemer, B. Biller, E. Choquet, M. A. Millar-Blanchaer, S. Sallum, B. Miles, N. Whiteford, P. Patapis, M. Perrin, L. Pueyo, G. Schneider, K. Stapelfeldt, J. Wang, K. Ward-Duong, B. P. Bowler, A. Boccaletti, J. H. Girard, D. Hines, P. Kalas, J. Kammerer, P. Kervella, J. Leisenring, E. Pantin, Y. F. Zhou, M. Meyer, M. C. Liu, M. Bonnefoy, T. Currie, M. McElwain, S. Metchev, M. Wyatt, O. Absil, J. Adams, T. Barman, I. Baraffe, M. Bonavita, M. Booth, M. Bryan, G. Chauvin, C. Chen, C. Danielski, M. De Furio, S. M. Factor, M. P. Fitzgerald, J. J. Fortney, C. Grady, A. Greenbaum, T. Henning, K. K. W. Hoch, M. Janson, G. Kennedy, M. Kenworthy, A. Kraus, M. Kuzuhara, P. O. Lagage, A. M. Lagrange, R. Launhardt, C. Lazzoni, J. Lloyd, S. Marino, M. Marley, R. Martinez, C. Marois, B. Matthews, E. C. Matthews, D. Mawet, J. Mazoyer, M. Phillips, S. Petrus, S. P. Quanz, A. Quirrenbach, J. Rameau, I. Rebollido, E. Rickman, M. Samland, B. Sargent, J. E. Schlieder, A. Sivaramakrishnan, J. M. Stone, M. Tamura, P. Tremblin, T. Uyama, M. Vasist, A. Vigan, K. Wagner and M. Ygouf, *Publ. Astron. Soc. Pac.*, 2022, **134**, 095003.
4 N. P. Ballering, L. I. Cleeves and D. E. Anderson, *Astrophys. J.*, 2021, **920**, 115.
5 M. Lecar, M. Podolak, D. Sasselov and E. Chiang, *Astrophys. J.*, 2006, **640**, 1115–1118.
6 K. Baillie, S. Charnoz and E. Pantin, *Astron. Astrophys.*, 2015, **577**, A65.
7 J. E. Owen, *Astrophys. J., Lett.*, 2014, **790**, L7.
8 N. van der Marel, R. B. Dong, J. di Francesco, J. P. Williams and J. Tobin, *Astrophys. J.*, 2019, **872**, 112.
9 A. D. Bosman, A. G. G. M. Tielens and E. F. van Dishoeck, *Astron. Astrophys.*, 2018, **611**, A80.
10 Y. Aikawa, in *Highlights of Astronomy*, ed. O. Engvold, Astronomical Soc Pacific, San Francisco, 2005, vol. 13, pp. 515–517.
11 C. Walsh, T. J. Millar, H. Nomura, E. Herbst, S. W. Weaver, Y. Aikawa, J. C. Laas and A. I. Vasyunin, *Astron. Astrophys.*, 2014, **563**, A33.
12 C. M. O. Alexander, L. R. Nittler, J. Davidson and F. J. Ciesla, *Meteorit. Planet. Sci.*, 2017, **52**, 1797–1821.
13 K. I. Oberg, V. V. Guzman, K. Furuya, C. H. Qi, Y. Aikawa, S. M. Andrews, R. Loomis and D. J. Wilner, *Nature*, 2015, **520**, 198–201.
14 M. K. McClure, C. Espaillat, N. Calvet, E. Bergin, P. D'Alessio, D. M. Watson, P. Manoj, B. Sargent and L. I. Cleeves, *Astrophys. J.*, 2015, **799**, 162.
15 O. Mousis, A. Aguichine, A. Bouquet, J. I. Lunine, G. Danger, K. E. Mandt and A. Luspay-Kuti, *Planet. Sci. J.*, 2021, **2**, 72.
16 A. M. A. Piso, J. Pegues and K. I. Oberg, *Astrophys. J.*, 2016, **833**, 203.
17 K. I. Oberg, A. C. A. Boogert, K. M. Pontoppidan, S. van den Broek, E. F. van Dishoeck, S. Bottinelli, G. A. Blake and N. J. Evans, *Astrophys. J.*, 2011, **740**, 109.
18 M. Rubin, C. Engrand, C. Snodgrass, P. Weissman, K. Altwegg, H. Busemann, A. Morbidelli and M. Mumma, *Space Sci. Rev.*, 2020, **216**, 102.
19 R. Martin-Domenech, G. M. Munoz Caro, J. Bueno and F. Goesmann, *Astron. Astrophys.*, 2014, **564**, A8.
20 S. Malyk, G. Kumi, H. Reisler and C. Wittig, *J. Phys. Chem. A*, 2007, **111**, 13365–13370.

21 K. Acharyya, G. W. Fuchs, H. J. Fraser, E. F. van Dishoeck and H. Linnartz, *Astron. Astrophys.*, 2007, **466**, 1005–1169.
22 G. W. Fuchs, K. Acharyya, S. E. Bisschop, K. I. Oberg, F. A. van Broekhuizen, H. J. Fraser, S. Schlemmer, E. F. van Dishoeck and H. Linnartz, *Faraday Discuss.*, 2006, **133**, 331–345.
23 J. L. Edridge, K. Freimann, D. J. Burke and W. A. Brown, *Philos. Trans. R. Soc., A*, 2013, **371**, 20110578.
24 A. Bar-Nun, D. Laufer, O. Rebolledo, S. Malyk, H. Reisler and C. Wittig, in *The Science of Solar System Ices*, ed. M. S. Gudipati and J. Castillo-Rogez, Springer, New York, 2013, vol. 356, ch. 14, pp. 487–499.
25 A. N. Greenberg, D. Laufer and A. Bar-Nun, *Mon. Not. R. Astron. Soc.*, 2017, **469**, S517–S521.
26 B. Muller, B. M. Giuliano, L. Bizzocchi, A. I. Vasyunin and P. Caselli, *Astron. Astrophys.*, 2018, **620**, A46.
27 S. Taj and M. R. S. McCoustra, *Mon. Not. R. Astron. Soc.*, 2020, **498**, 1693–1699.
28 *Faraday Discuss.*, 2006, **133**, 347–374.
29 M. P. Collings, J. W. Dever, H. J. Fraser, M. R. S. McCoustra and D. A. Williams, *Astrophys. J.*, 2003, **583**, 1058–1062.
30 E. C. Fayolle, K. I. Oberg, H. M. Cuppen, R. Visser and H. Linnartz, *Astron. Astrophys.*, 2011, **529**, A74.
31 M. P. Collings, J. W. Dever and M. R. S. McCoustra, *Chem. Phys. Lett.*, 2005, **415**, 40–45.
32 H. J. Fraser, M. P. Collings, J. W. Dever and M. R. S. McCoustra, *Mon. Not. R. Astron. Soc.*, 2004, **353**, 59–68.
33 M. P. Collings, M. A. Anderson, R. Chen, J. W. Dever, S. Viti, D. A. Williams and M. R. S. McCoustra, *Mon. Not. R. Astron. Soc.*, 2004, **354**, 1133–1140.
34 K. Isokoski, J. B. Bossa, T. Triemstra and H. Linnartz, *Phys. Chem. Chem. Phys.*, 2014, **16**, 3456–3465.
35 B. Mate, O. Galvez, B. Martin-Llorente, M. A. Moreno, V. J. Herrero, R. Escribano and E. Artacho, *J. Phys. Chem. A*, 2008, **112**, 457–465.
36 D. M. Hudgins, S. A. Sandford, L. J. Allamandola and A. Tielens, *Astrophys. J., Suppl. Ser.*, 1993, **86**, 713–870.
37 P. A. Gerakines, W. A. Schutte, J. M. Greenberg and E. F. Vandishoeck, *Astron. Astrophys.*, 1995, **296**, 810–818.
38 P. A. Gerakines and R. L. Hudson, *Astrophys. J., Lett.*, 2015, **808**, L40.
39 B. M. Giuliano, R. M. Escribano, R. Martin-Domenech, E. Dartois and G. M. Munoz Caro, *Astron. Astrophys.*, 2014, **565**, A108.
40 A. Kouchi and T. Yamamoto, *Prog. Cryst. Growth Charact. Mater.*, 1995, **30**, 83–108.
41 R. Feistel and W. Wagner, *Geochim. Cosmochim. Acta*, 2007, **71**, 36–45.
42 A. Kouchi and S. Sirono, *Geophys. Res. Lett.*, 2001, **28**, 827–830.
43 R. S. Smith, J. Matthiesen, J. Knox and B. D. Kay, *J. Phys. Chem. A*, 2011, **115**, 5908–5917.
44 M. Chonde, M. Brindza and V. Sadtchenko, *J. Chem. Phys.*, 2006, **125**, 094501.
45 Y. P. Handa, O. Mishima and E. Whalley, *J. Chem. Phys.*, 1986, **84**, 2766–2770.
46 A. Guilbert-Lepoutre, S. Besse, O. Mousis, M. Ali-Dib, S. Hoefner, D. Koschny and P. Hager, *Space Sci. Rev.*, 2015, **197**, 271–296.
47 A. Guilbert-Lepoutre, A. Gkotsinas, S. N. Raymond and D. Nesvorny, *Astrophys. J.*, 2023, **942**, 92.

48 R. M. Escribano, G. M. M. Caro, G. A. Cruz-Diaz, Y. Rodriguez-Lazcano and B. Mate, *Proc. Natl. Acad. Sci. U. S. A.*, 2013, **110**, 12899–12904.
49 M. Drahus, B. Yang, D. C. Lis and D. Jewitt, *Mon. Not. R. Astron. Soc.*, 2017, **468**, 2897–2909.
50 D. Jewitt, *Astron. J.*, 2009, **137**, 4296–4312.
51 B. J. R. Davidsson, N. H. Samarasinha, D. Farnocchia and P. J. Gutierrez, *Mon. Not. R. Astron. Soc.*, 2022, **509**, 3065–3085.
52 R. E. Mastrapa, W. Grundy and M. Gudipati, in *The Science of Solar System Ices*, ed. M. S. Gudipati and J. Castillo-Rogez, Springer, New York, 2013, vol. 356, ch. 11, pp. 371–408.
53 C. Herny, O. Mousis, R. Marschall, N. Thomas, M. Rubin, O. Pinzón-Rodríguez and I. P. Wright, *Planet. Space Sci.*, 2021, **200**, 105194.
54 M. Hoang, P. Garnier, H. Gourlaouen, J. Lasue, H. Reme, K. Altwegg, H. Balsiger, A. Beth, U. Calmonte, B. Fiethe, A. Galli, S. Gasc, A. Jackel, A. Korth, L. Le Roy, U. Mall, M. Rubin, T. Semon, C. Y. Tzou, J. H. Waite and P. Wurz, *Astron. Astrophys.*, 2019, **630**, A33.
55 C. Tubiana, G. Rinaldi, C. Guttler, C. Snodgrass, X. Shi, X. Hu, R. Marschall, M. Fulle, D. Bockeele-Morvan, G. Naletto, F. Capaccioni, H. Sierks, G. Arnold, M. A. Barucci, J. L. Bertaux, I. Bertini, D. Bodewits, M. T. Capria, M. Ciarniello, G. Cremonese, J. Crovisier, V. Da Deppo, S. Debei, M. De Cecco, J. Deller, M. C. De Sanctis, B. Davidsson, L. Doose, S. Erard, G. Filacchione, U. Fink, M. Formisano, S. Fornasier, P. J. Gutierrez, W. H. Ip, S. Ivanovski, D. Kappel, H. U. Keller, L. Kolokolova, D. Koschny, H. Krueger, F. La Forgia, P. L. Lamy, L. M. Lara, M. Lazzarin, A. C. Levasseur-Regourd, Z. Y. Lin, A. Longobardo, J. J. Lopez-Moreno, F. Marzari, A. Migliorini, S. Mottola, R. Rodrigo, F. Taylor, I. Toth and V. Zakharov, *Astron. Astrophys.*, 2019, **630**, A23.
56 U. Fink, L. Doose, G. Rinaldi, A. Bieler, F. Capaccioni, D. Bockelee-Morvan, G. Filacchione, S. Erard, C. Leyrat, M. Blecka, M. T. Capria, M. Combi, J. Crovisier, M. C. De Sanctis, N. Fougere, F. Taylor, A. Migliorini and G. Piccioni, *Icarus*, 2016, **277**, 78–97.
57 M. Hoang, P. Garnier, J. Lasue, H. Rème, M. T. Capria, K. Altwegg, M. Läuter, T. Kramer and M. Rubin, *Astron. Astrophys.*, 2020, **638**, A106.
58 R. S. Smith, C. Huang, E. K. L. Wong and B. D. Kay, *Phys. Rev. Lett.*, 1997, **79**, 909.
59 R. S. Smith, C. Huang and B. D. Kay, *J. Phys. Chem. B*, 1997, **101**, 6123–6126.
60 K. L. Heritier, K. Altwegg, J. J. Berthelier, A. Beth, C. M. Carr, J. De Keyser, A. I. Eriksson, S. A. Fuselier, M. Galand, T. I. Gombosi, P. Henri, F. L. Johansson, H. Nilsson, M. Rubin, C. S. Wedlund, M. G. G. T. Taylor and E. Vigren, *Nat. Commun.*, 2018, **9**, 2580.
61 A. Bieler, K. Altwegg, H. Balsiger, A. Bar-Nun, J. J. Berthelier, P. Bochsler, C. Briois, U. Calmonte, M. Combi, J. De Keyser, E. F. van Dishoeck, B. Fiethe, S. A. Fuselier, S. Gasc, T. I. Gombosi, K. C. Hansen, M. Hassig, A. Jackel, E. Kopp, A. Korth, L. Le Roy, U. Mall, R. Maggiolo, B. Marty, O. Mousis, T. Owen, H. Reme, M. Rubin, T. Semon, C. Y. Tzou, J. H. Waite, C. Walsh and P. Wurz, *Nature*, 2015, **526**, 678–681.
62 J. R. Spencer, W. M. Calvin and M. J. Person, *J. Geophys. Res.: Planets*, 1995, **100**, 19049–19056.
63 B. D. Teolis, J. Shi and R. A. Baragiola, *J. Chem. Phys.*, 2009, **130**, 134704.

64 J. R. Berdis, M. S. Gudipati, J. R. Murphy and N. J. Chanover, *Icarus*, 2020, **341**, 113660.
65 A. V. Oza, F. Leblanc, R. E. Johnson, C. Schmidt, L. Leclercq, T. A. Cassidy and J. Y. Chaufray, *Planet. Space Sci.*, 2019, **167**, 23–32.
66 Y. Ashkenazy, *Heliyon*, 2019, **5**, e01908.
67 J. A. Rathbun, N. J. Rodriguez and J. R. Spencer, *Icarus*, 2010, **210**, 763–769.